MATERIALS SCIENCE

Nondestructive imaging of atomically thin nanostructures buried in silicon

Georg Gramse,[1]* Alexander Kölker,[2,3] Tingbin Lim,[2] Taylor J. Z. Stock,[2] Hari Solanki,[2] Steven R. Schofield,[2,4] Enrico Brinciotti,[5] Gabriel Aeppli,[6,7,8,9] Ferry Kienberger,[5] Neil J. Curson[2,3]*

It is now possible to create atomically thin regions of dopant atoms in silicon patterned with lateral dimensions ranging from the atomic scale (angstroms) to micrometers. These structures are building blocks of quantum devices for physics research and they are likely also to serve as key components of devices for next-generation classical and quantum information processing. Until now, the characteristics of buried dopant nanostructures could only be inferred from destructive techniques and/or the performance of the final electronic device; this severely limits engineering and manufacture of real-world devices based on atomic-scale lithography. Here, we use scanning microwave microscopy (SMM) to image and electronically characterize three-dimensional phosphorus nanostructures fabricated via scanning tunneling microscope–based lithography. The SMM measurements, which are completely nondestructive and sensitive to as few as 1900 to 4200 densely packed P atoms 4 to 15 nm below a silicon surface, yield electrical and geometric properties in agreement with those obtained from electrical transport and secondary ion mass spectroscopy for unpatterned phosphorus δ layers containing ~10^{13} P atoms. The imaging resolution was 37 ± 1 nm in lateral and 4 ± 1 nm in vertical directions, both values depending on SMM tip size and depth of dopant layers. In addition, finite element modeling indicates that resolution can be substantially improved using further optimized tips and microwave gradient detection. Our results on three-dimensional dopant structures reveal reduced carrier mobility for shallow dopant layers and suggest that SMM could aid the development of fabrication processes for surface code quantum computers.

INTRODUCTION

Semiconductor nanostructures consisting of areas of buried dopant atom(s) are crucial components for present and future complementary metal-oxide semiconductor transistor technologies (1), as well as for emerging quantum computing architectures (2, 3). Depending on their size and shape, they can produce quantum confinement in one, two, or three dimensions, which may be exploited for device operation. Consequently, noninvasive imaging and electrical characterization of buried nanostructures, with precise lateral and depth resolution, would be of great value for the development and inspection of integrated circuits and quantum devices.

Over the last decade, the technique of hydrogen resist lithography, which uses a scanning tunneling microscope (STM) to pattern a hydrogen passivation layer, has proved ideal for the definition of laterally confined atomically thin two-dimensional (2D) phosphorus (P) dopant nanostructures. Nanoscale P sheets (4), wires (5), and dots (6) have all been fabricated. These buried nanoscale structures challenge techniques aimed at determining electrical and geometrical properties of subsurface devices. STM itself offers only limited subsurface sensitivity (7) for imaging and no ability to determine the sheet resistivity of the nanostructures or their depth beneath the surface. In contrast, scanning probe microscopy techniques based on applying alternating electric fields and probing the local impedance are more useful for subsurface imaging because the field penetrates further. Established methods, such as electrostatic

force microscopy (EFM) and scanning capacitance microscopy, measure capacitances at kilohertz and megahertz frequencies and are capable of imaging subsurface features (8–10); however, the data provide only qualitative image contrast. Here, we show that scanning microwave microscopy (SMM), which operates at higher frequencies (1 to 20 GHz) and can measure the complex impedance of the buried nanostructures, gives access to both dielectric (11–14) and conductivity (15–17) properties, including, in particular, those due to dopants (16, 18–21). Unlike destructive imaging techniques such as focused ion beam milling combined with scanning electron microscopy (22), transmission electron microscopy (TEM) (23), and secondary ion mass spectrometry (SIMS) (24), SMM experiments can be performed with virtually no sample modification, in an ambient environment, using a standard atomic force microscope (AFM) (25) or STM (26) combined with a vector network analyzer (VNA) (27) or custom-made electronics (28). Typically, resonators (29) or matching circuits (28), as well as simpler direct connections (30, 31), are used to sense the minute electrical changes that come from the SMM probe. Recently, it has been shown that SMM is capable of visualizing buried conducting structures (20, 21, 32) and differently doped bulk regions buried below an insulating layer (33). Here, we demonstrate the capability to determine the 3D disposition and electrical characteristics of atomically thin buried phosphorus nanostructures formed by incorporation and encapsulation of substitutional P atoms within multiple layers in a Si crystal. Using optimized growth parameters, the layers are densely packed (1.4 atoms/nm^2) and can be confined to widths of a few nanometers, with near 100% carrier activation, within the confined region (34). The capabilities demonstrated here are transformative for noninvasive diagnostics of atomic-scale electric components that will form the next generation of "classical" and quantum devices.

Figure 1 shows the SMM setup, and Materials and Methods explains its operation. Briefly, a VNA connected to a conducting AFM probe transmits an electromagnetic wave to the probe and detects the reflected wave. The ratio of the incident and the reflected signal power (the

[1]Johannes Kepler University, Biophysics Institute, Gruberstrasse 40, 4020 Linz, Austria. [2]London Centre of Nanotechnology, University College London (UCL), 17-19 Gordon Street, London WC1H 0AH, UK. [3]Department of Electronic and Electrical Engineering, UCL, Torrington Place, London WC1E 7JE, UK. [4]Department of Physics and Astronomy, UCL, Gower Street, London WC1E 6BT, UK. [5]Keysight Laboratories, Keysight Technologies Inc., Gruberstrasse 40, 4020 Linz, Austria. [6]Department of Physics, ETH, Zurich CH-8093, Switzerland. [7]Institut de Physique, École polytechnique fédérale de Lausanne, Lausanne CH-1015, Switzerland. [8]Paul Scherrer Institut, Villigen CH-5232, Switzerland. [9]Bio Nano Consulting, Gridiron Building, One Pancras Square, London N1C 4AG, UK.
*Corresponding author. Email: georg.gramse@jku.at (G.G.); n.curson@ucl.ac.uk (N.J.C.)
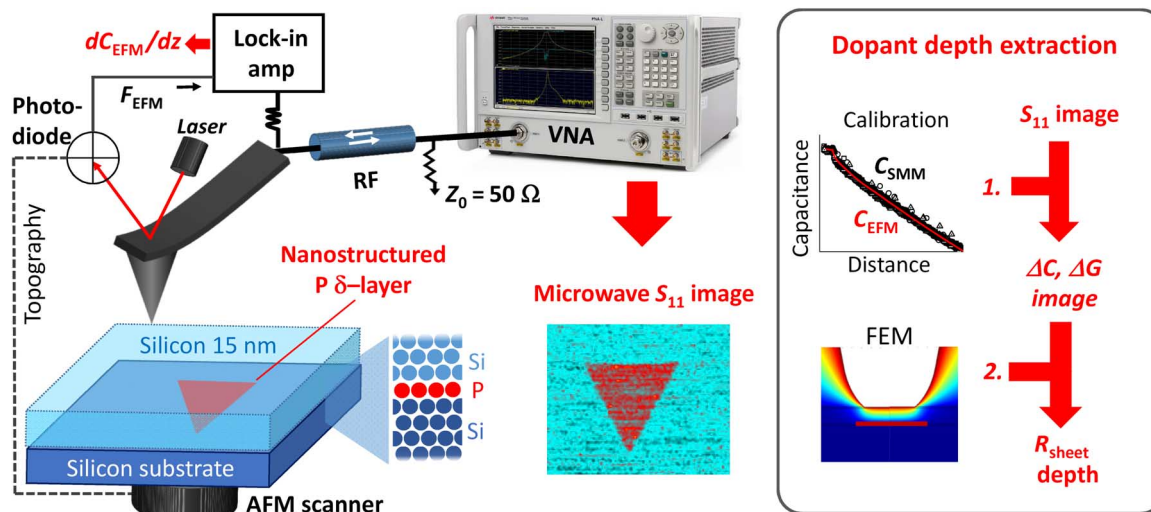
Fig. 1. SMM experimental setup and workflow for calibrated impedance measurements and dopant depth extraction of buried 2D phosphorus layers. VNA measures local S_{11} reflection coefficient (amplitude and phase). For calibration, dC_{EFM}/dz signal is detected by a lock-in amplifier. Workflow for dopant depth extraction shown in (1) SMM S_{11} images/curves are calibrated (13) to obtain quantitative complex admittance data, $Y = G + i\omega C$, with C as the capacitance, G as the conductance, ω as the angular frequency, and $i^2 = -1$. (2) FEM is used to extract sheet resistance and depth from the admittance signal. RF, microwave signal.

complex S_{11} reflection parameter) gives information on the local sample properties below the probe. High sensitivity to variations in the sheet resistivity of P dopant layers is obtained by operating the SMM at $f \sim 20$ GHz (see section S1 and fig. S1). Quantitative depth and conductivity parameters of the P layer are obtained by suitable calibration processes (13) combined with robust finite element modeling (FEM) in the illustrated two-step procedure.

RESULTS

SMM detection of buried phosphorus

Patterns consisting of a single phosphorus layer (δ layer) have been written onto the silicon substrate, as detailed in Materials and Methods. The AFM contact mode topography image acquired after subsequent encapsulation with ~15 nm of Si (Fig. 2A) shows a hardly visible height difference of ~0.2 nm for the square of the incorporated phosphorus, which can be attributed to a slightly increased surface roughness within the nanostructured area.

In contrast, the calibrated SMM capacitance image shown in Fig. 2B exhibits a clearly visible, positive contrast of $\Delta C = 2.1 \pm 0.1$ aF for the nanostructured phosphorus square with respect to the surrounding substrate. This can also be seen from the profile in Fig. 2E. Although the feature height is close to the SMM noise floor of $C_{noise} \sim 0.1\,\text{aF}/\sqrt{\text{Hz}}$ corresponding to $C_{noise} \sim 1$ aF at a chosen scan speed of 0.4 lines/s, the image is still very clear and several line profiles can be averaged to further reduce the noise. In addition to the capacitance signal, we also observe a very small contrast in the conductance channel that is difficult to see in the image (Fig. 2E). This signal is in the same range as the noise floor, $\Delta G_{noise} \sim 100$ nS; however, the contrast of $\Delta G = 25 \pm 15$ nS could be estimated after averaging individual line profiles taken across the entire square, as shown in Fig. 2F.

We have also performed a control experiment where two lithographic patches were fabricated, but only one of them was dosed with phosphine (by creating the second patch subsequent to the PH_3 exposure step). These are the two triangular patches shown in Fig. 2 (G to I), where only the left triangle was exposed to PH_3. After a silicon coverage of

~15 nm, the measured AFM topography contrast (Fig. 2G) for the depassivated triangle is ~0.6 nm, in contrast to only ~0.2 nm for the phosphorus-incorporated triangle. This relative height difference of 0.4 nm corresponds to about three layers of Si and indicates an inherent change in Si growth on the P and H patterned regions. The rate of homoepitaxial growth of Si is sensitive to small coverages of surface hydrogen (35), and a low coverage of residual H is likely to remain in the patterned region. The hydrogen desorbed triangle in Fig. 2H shows no measurable capacitance contrast in the image, confirming the absence of phosphorus and its consequent electronic effects at the hydrogen depassivated triangle. Furthermore, we note that the 0.6 nm roughness increase in the desorbed triangle is not detected in the SMM capacitance channel, that is, crosstalk between the capacitance and the surface roughness is negligible.

P depth and conductivity extraction

The SMM contrast is markedly stronger in the capacitance channel than the conductance channel. The capacitance contrast results from the buried dopant nanostructures forming local conducting planes below the surface such that a capacitance, $C = \varepsilon A/d$, is built up between the buried plane and the conducting probe apex, where A is the physical contact area between the probe tip and the substrate surface, d is the depth, and ε is the Si dielectric constant. For the substrate, the measured capacitance must be lower because it is governed by the width of the depletion layer, which is much larger than the P-layer depth (for details, see section S2) (36).

For a quantitative interpretation, which is required to extract the exact depth of the phosphorus layer and its conductivity, this simple picture has to be refined by also taking into account the precise geometry of the system and the dopants in the substrate. We have used FEM to calculate the theoretical admittance of the model shown in Fig. 3A. The phosphorus is modeled as a thin layer (0.2 nm) with a conductivity, σ_P, embedded at a depth, h, in the depletion layer of the low-doped silicon substrate. The basis for the assumed layer thickness is justified by the data shown in fig. S1 and associated text. Figure 3B shows the voltage distribution for this model with (left) and without (right) the highly conductive layer present. The voltage profile along the symmetry axis in
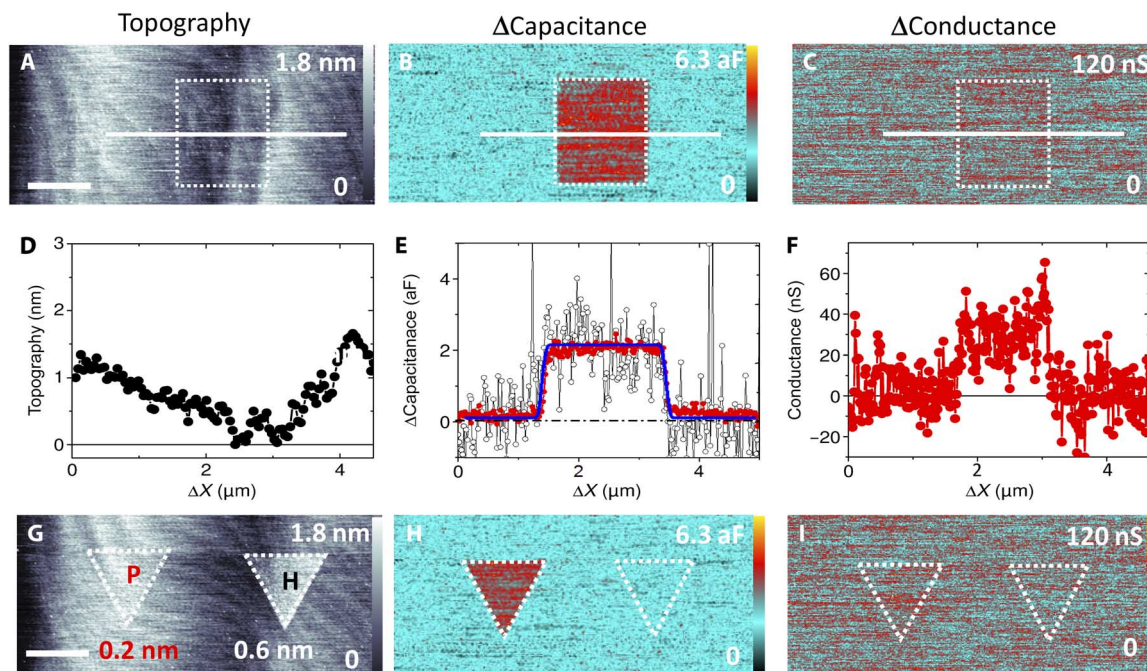
Fig. 2. SMM imaging of patterned phosphorus δ layers buried via epitaxy on Si(100) wafers. (A) AFM topography after coverage with 15 nm of Si. (B) SMM capacitance image showing clear contrast for the phosphorus pattern. (C) SMM conductance image. Corresponding line profiles are shown in (D), (E), and (F), respectively. Line profile across the square pattern (black, single line; red, 10 lines averaged; blue, fit with logistic function). (G) AFM topography image of patterned phosphorus (P) layer and depassivated hydrogen (H) layer. Corresponding (H) capacitance and (I) conductance images. Scale bars, 1.4 μm; VNA power, 1 dBm; f = 19.81 GHz; scan speed, 0.4 lines/s (512 points).

Fig. 3C validates the initial assumption that, essentially, the entire potential drops off in the h = 15 nm between the tip and the buried phosphorus nanostructure. For the case where no phosphorus is present, the potential decays much more slowly within the substrate, leading to a lower capacitance. Because the size of the probe tip is just a few tens of nanometers, most of the potential in the depletion layer decays in the first few hundred nanometers below the surface, indicating that, for small probe tips, the technique is most sensitive to the near subsurface, as also discussed in section S2 and by Fumagalli *et al.* (*37*) and Gramse *et al.* (*38*). For a quantitative extraction of the dopant layer depth, the tip geometry and contact area between the conducting tip and sample are essential properties that need to be established experimentally. Therefore, we fit simulated capacitances to a capacitance versus distance curve on the bare Si substrate obtained directly after imaging the nanostructure (fig. S2). The free parameters in this fitting procedure are the apex radius, cone angle, and contact radius of the circular contact area, which are determined to be r_a = 20 ± 5 nm, θ = 8° ± 1°, and r_c = 11 ± 2 nm, respectively. The first two parameters are extracted from the out-of-contact region of the approach curve, whereas r_c is determined from the region where the tip is already in contact with the substrate (for details, see section S2). The extracted values are within the nominal 10- to 30-nm range of values provided by the tip manufacturer (*39*). Measurements carried out using a blunter tip (as shown in fig. S2B) give a clearly larger capacitance, proving the importance of the precise tip geometry.

After having defined all the geometrical parameters in the model, the depth of the dopant layer and its conductivity can be extracted by comparing the experimental capacitance and conductance images (Fig. 2) with the simulated values. Therefore, in Fig. 3 (E and F), the simulated capacitance and conductance differences (P δ-layer ground plane minus substrate) are shown as a function of the phosphorus layer conductivity for dopant depths of h = 15 nm (solid line) and h = 10 nm/20 nm, respectively (dotted lines). The experimentally obtained values are shown as red dots and result in a dopant layer depth of h = 15 ± 1 nm and a conductivity of σ_1 = 1.2 × 10^6 S/m. Although the SMM measurement frequency has been chosen for sensitivity to variations for the highly (>10^3 S/m) conductive P dopant layers, the decreasing sensitivity at >10^5 S/m (cf. Fig. 3, E and F, and fig. S1) leads to larger confidence intervals of (10^5 to 10^8) S/m. This is not surprising because it is in the metallic regime. However, by using larger tip radii (fig. S2B and Fig. 3G), we are able to decrease the confidence interval and extract h = 14 ± 1 nm and σ_2 = 3 × 10^6 S/m with (2 × 10^6 to 5 × 10^6) S/m. Equalizing the simulated and measured complex admittance values means that two constraints have to be met, so that both phosphorus conductivity and dopant depth can be extracted clearly and without ambiguity. This can be observed also by the additional representation of the capacitance and conductance data in the complex plane for small (Fig. 3F) and large (Fig. 3G) tips.

Application to 3D P δ-layer structure

We have applied the SMM imaging capabilities to an advanced δ-layer structure, as shown in Fig. 4A. This complex structure consists of two overlaid perpendicular sets of three phosphorus-doped bars. Each set of bars was prepared in the same manner using three different PH$_3$ doses, one for each bar, leading to different doping densities as indicated. A separation layer of approximately 5 nm of Si was grown between the patterned sets of the bars, such that the overlaid sets of bars reside at depths of h = 8.9 nm and h = 4 nm below the surface (as verified by SIMS measurements on an unpatterned double δ-layer sample fabricated using the same growth parameters; see section S3 and fig. S4). The SMM
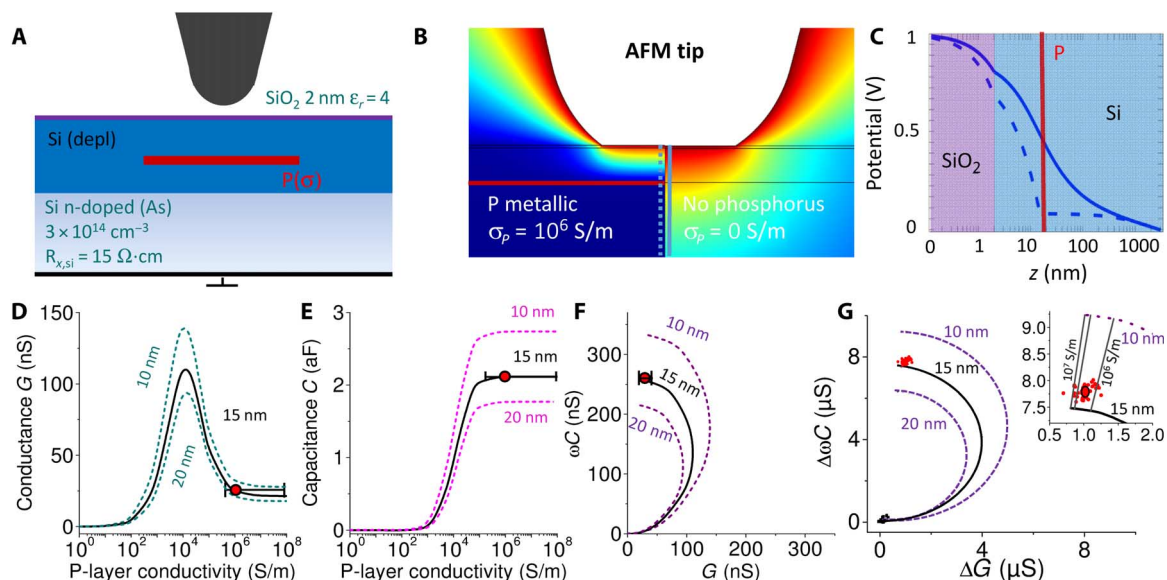
Fig. 3. Depth and conductivity extraction for the P δ layer. (**A**) Sketch of axisymmetric finite element model used to calculate theoretical SMM admittance. depl, depletion. (**B**) Potential distribution for simulated model: tip in contact with bare Si substrate (right) and P δ layer present 15 nm below the surface (left). (**C**) Corresponding voltage profiles in z direction parallel to the tip symmetry axis for a 20-nm tip (solid line, bare substrate; dashed line, with phosphorus layer). (**D** and **E**) Modeled capacitance (ΔC) and conductance (ΔG) dependence on phosphorus layer conductivity calculated for a dopant depth of $h = 15$ nm (solid line) and $h = (15 \pm 5)$ nm (dotted and colored lines) for tip $r_a = 20$ nm. Experimental value (red dot) is shown in the graphs for extraction of dopant depth and P-sheet conductivity. (**F**) Representation of ΔC and ΔG in complex plane. (**G**) Measurement with larger probe ($r_a = 290 \pm 1$ nm): Representation of $\Delta \omega C$ and ΔG in complex plane. Here, we show the scatter of the data rather than the averaged data over all values as we did for (D) to (F). Layer depth and conductivity are extracted from the inset showing a zoom-in of (G). Note that the dependency on the layer conductivity and depth is visualized.

capacitance image in Fig. 4B shows a good contrast between the top and bottom levels, whereas the topography image is completely uncorrelated with the capacitance (see more details in fig. S5), except on bar B1 where the measurement has been hindered by surface modification during the lithography process. In particular, the bottom bar B3 shows a clear decrease in capacitance contrast (see line profiles in Fig. 4, C and D). The quantification of the dopant depth and concentration was carried out, as detailed above, but with a full 3D model (Fig. 4A). To this end, the experimental admittance data extracted from Fig. 4 (C and D) are plotted in Fig. 4E, together with the simulated values in the complex admittance plane. Note that we excluded bar B1 in this analysis because of the surface modification. The top levels agree well with a depth of $h_{T1} = 4.3 \pm 0.5$ nm, $h_{T2} = 4.5 \pm 0.5$ nm, and $h_{T3} = 4.2 \pm 0.5$ nm, and also the depth of bottom levels of $h_{B2} = 8.2 \pm 0.7$ nm and $h_{B3} = 9.6 \pm 0.7$ nm can be still extracted, however, with lower accuracy. The extracted conductivities are $\sigma_{B2} = (1 \pm 0.2) \times 10^6$ S/m and $\sigma_{B3} = (0.7 \pm 0.1) \times 10^6$ S/m and, for the top levels, $\sigma_{T1} = (0.7 \pm 0.1) \times 10^6$ S/m, $\sigma_{T2} = (0.65 \pm 0.1) \times 10^6$ S/m, $\sigma_{T3} = (0.62 \pm 0.1) \times 10^6$ S/m.

Lateral resolution and sensitivity

The sensitivity to buried and isolated P atoms and the capability to laterally resolve fine P patterns are two key features of the technique. The lateral resolution was derived from the capacitance line profile in Fig. 2E, which was fitted with a difference of two logistic functions, $f_{\text{logis}}(x) = A\left(1 + e^{-(x-x_0)/\delta}\right)^{-1} - A\left(1 + e^{-(x-x_1)/\delta}\right)^{-1}$, where A, δ, x_0, and x_1 are the fitting parameters and δ defines the sharpness of the step. From this fit, the width of the step from Si to P has been estimated to be $\text{Res}_{50-88,C} = 2\delta = 55 \pm 4$ nm. For the shallower 3D structures in Fig. 4, we find an improvement to $\delta_B = 47 \pm 3$ nm for the bottom layer and $\delta_T = 37 \pm 1$ nm for the top layer, notwithstanding that we also used here a bigger tip radius to increase the accuracy of the extracted R_{sheet}.

From measurements on fine patterns (see fig. S6 and section S4), we found that isolated features as small as 10 nm buried at 15 nm can still be detected; however, they appear broadened in the capacitance image. To obtain a quantitative estimate of the feature size that can be resolved in more complex and dense circuits, five pairs of stripes with increasing pitch have been patterned (200, 150, 100, 70, and 30 nm) and buried below 15 nm of Si. The SMM capacitance image in Fig. 5A and the corresponding line profile in Fig. 5B demonstrate that the stripes separated by 70 nm can still be resolved, in agreement with the previous observation. At 30-nm separation, the SMM does not distinguish the individual stripes.

The fit of capacitance curves from 3D finite element simulations to the experimental data yielded the same apex but a slightly increased contact radius indicative for tip wear typically observed after prolonged scanning. Overall, the simulated data agree well with the experiment, and only at low separations, $L = 30$ to 70 nm, a minor difference between experiment and simulation is visible. The effect of the two parameters defining the lateral resolution, namely, the depth of the dopant layer, h, and the apex radius, r_a, has been modeled, as shown in Fig. 5 (C to F).

For stripes with a pitch of 100 nm, the depth was varied from $h = 5$ nm to $h = 100$ nm, showing a clear increase (decrease) of the contrast for lower (higher) Si coverage, as expected. Assuming an SMM capacitance sensitivity of 0.5 aF (bandwidth, 25 Hz), the maximum resolvable feature separation, L, has been calculated from the data in Fig. 5C as a function of the depth. For a dopant depth of $h = 5$ nm, the SMM should clearly resolve separations of $d = 40$ nm, as we also observe in our experiments, whereas at $h = 40$ nm, it is expected to have only submicrometer lateral resolution, as can be seen in Fig. 5D. Simulations with varying tip radius in Fig. 5 (E and F) show that the lateral resolution does not increase monotonically with decreasing tip radius. There is rather an optimum contact radius, which is in the range of 30 to
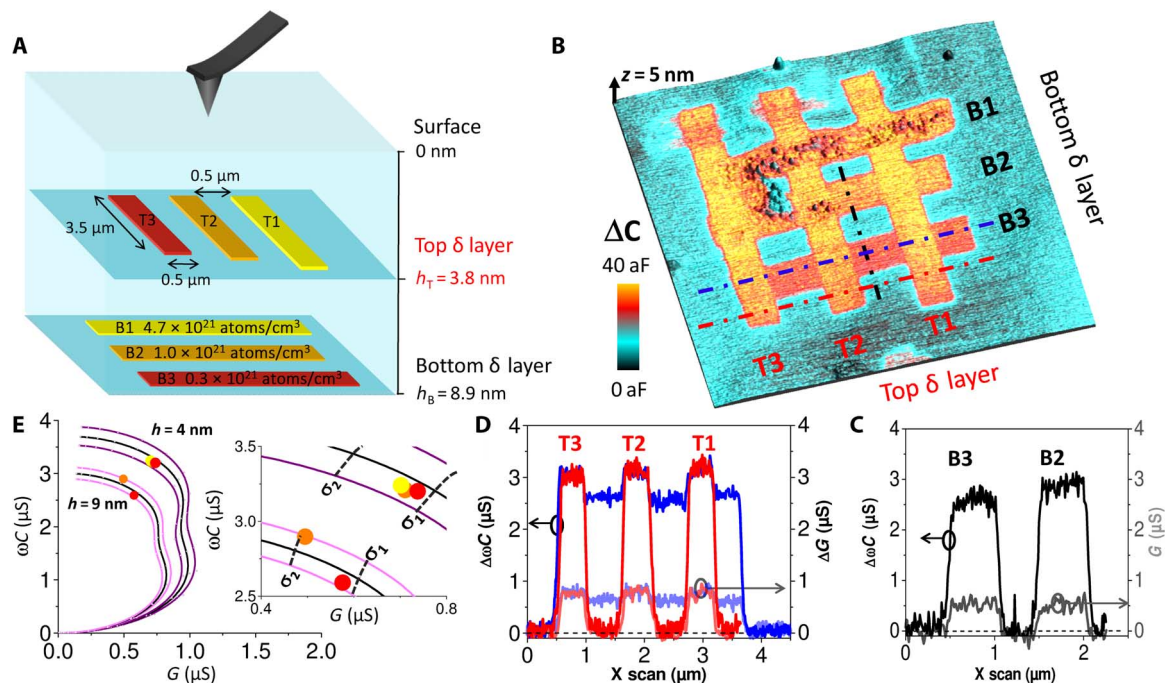
Fig. 4. 3D P δ-layer structure depth and conductivity extraction. (**A**) Sketch of 3D structure comprising three bars with increased dosing (coded by same colors for both layers) at two different heights, as indicated and verified by SIMS. (**B**) AFM 3D topography image with SMM capacitance signal as color overlay (image size, 5.4 μm × 5.4 μm × 5 nm). (**C** and **D**) ΔωC and ΔG line profiles, allowing contributions from different device layers to be identified, extracted from positions indicated in (B). (**E**) Modeled admittance (capacitance ΔωC and conductance ΔG) in dependence of phosphorus layer conductivity σ for dopant depth $h = 4$ nm and $h = 9$ nm (solid black lines) and for ±1 nm of these values (purple lines). Experimental values (red, orange, and yellow dots) extracted from (D) and (C) are shown in the graphs for extraction of dopant depth and P-sheet conductivity. Inset shows zoom-in for the extraction of depth and phosphorus layer conductivity from simulations (dashed lines mark layer conductivities of $\sigma_1 = 0.6 \times 10^6$ S/m and $\sigma_2 = 1 \times 10^6$ S/m). (Measurement frequency $f = 19.83$ GHz; power, 0 dBm; tip radius $r_a = 173$ nm.)

40 nm (cp. Fig. 5F). For tip radii above 100 nm, the contrast is inverted and individual stripes are not resolved anymore. The obtained simulation results can be understood, taking into account that not only the tip apex but also the less local cone is contributing to the capacitance signal (for details, see section S4 and fig. S7). For tip radii less than 30 nm, the tip apex contributes less than the cone to the signal, leading to a decrease in lateral resolution. Currently, a calibrated detection scheme is under development, which uses microwave gradient detection to cancel out the cone contribution.

Concerning the detection sensitivity for isolated P atoms, we estimate from the observed lateral resolution Res and the density $\rho_P = 1.4$ atoms/nm^2 (40, 41) of P atoms in the subsurface layer that as few as Res$^2 \rho_P \sim 4200$ atoms can be detected at a bandwidth of 10 Hz. This estimate is supported by finite element simulations, suggesting that 4600 P atoms at $h = 15$ nm are enough for detection by the SMM (see fig. S6C and section S4), which reduces to 1500 atoms at $h = 5$ nm.

DISCUSSION
We have demonstrated SMM, which combines AFM as a nanoscale investigation technique and the VNA for quantitative microwave measurements, to be an excellent tool for locating and investigating buried electronic features. The novel characteristics of the technique are that it is noninvasive, enables location of features in three dimensions with high resolution, and provides their quantitative electrical characteristics. In particular, atomically thin δ layers of phosphorus, patterned by STM hydrogen desorption lithography and buried below 15 nm of Si, are easily resolvable and quantitatively characterizable using SMM. These

layers are known to form subsurface 2D electron gases exhibiting quasi-metallicity and weak localization (42, 43); determining their sheet resistance via ordinary dc techniques is challenging because of the need to establish the appropriate electrical contacts and is even more difficult at room temperature where other current paths contribute to the electrical transport. The extracted depth of 14 ± 1 nm and sheet resistance of $R_{sheet} = 1.7 \pm 0.7$ kilohms per square compare favorably with similar values measured for phosphorus δ-layer samples fabricated in an identical way but without the H lithographic step (see Materials and Methods). SIMS measurements on these samples determined a depth of 14.45 ± 0.01 nm. Hall bar measurements, also made on the unpatterned samples, measured a sheet resistance of 1.4 ± 0.1 kilohms per square.

The application of SMM to more complex 3D structures consisting of two layers separated by only 5 nm shows the practical use of the technique to assess the quality in terms of electrical conductivity and distinguish different doping levels and depths of the δ layers. The extracted depth of both layers $h_B = 8$ to 10 nm and $h_T = 4$ nm shows a very good agreement with SIMS measurements (see fig. S4). Although the maximum P density is identical to the one used in measurements of Fig. 2, for the 3D sample, we observe an R_{sheet} of 5 to 8 kilohms per square, which is significantly higher than on the single-layer sample buried below 15 nm of Si. On the one hand, this quantitative difference in R_{sheet} might suggest a reduced P activation and/or Si homogeneity that is expected because of the more complex preparation procedure, which includes the use of locking layers (44). On the other hand, our results would support the findings of Clarke et al. (45), which suggest a 40% lower carrier density from carriers located at dopants closer to the surface (4 nm) compared to those at 9 nm. The latter explanation would
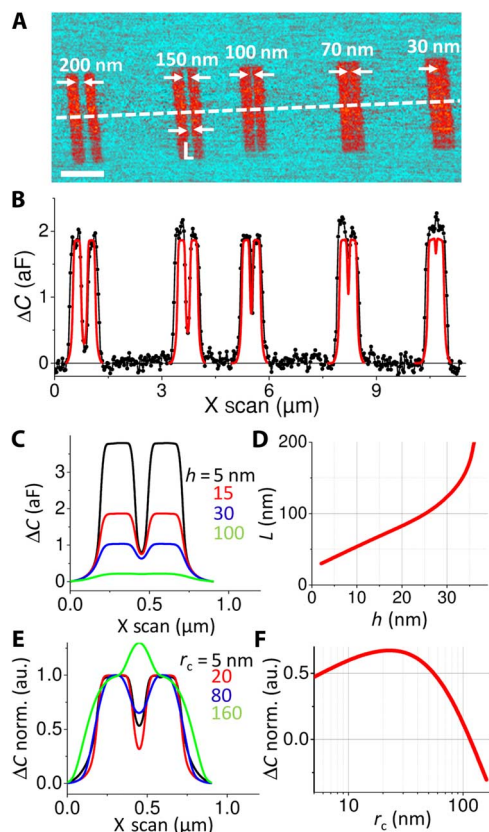
Fig. 5. SMM capacitance subsurface lateral resolution. (**A**) SMM capacitance image of stripes and (**B**) corresponding capacitance line profile (black dots, 10 lines averaged) including simulated capacitance for corresponding phosphorus stripes assuming h = 15-nm depth below surface, apex radius r_a = 20 nm, and contact radius r_c = 12 nm (VNA power, 1 dBm; f = 19.05 GHz). (**C**) Simulated capacitance profile for phosphorus structure at h = 5-, 15-, 30-, and 100-nm depth (separation, L = 100 nm). (**D**) Resolvable P feature separations as a function of the layer depth (for an SMM sensitivity of 0.5 aF). (**E**) Normalized simulated capacitance profiles of P stripes in dependency of contact radius (L = 100 nm). au., arbitrary units. (**F**) Normalized capacitance contrast from (E) as a function of contact radius r_c (Note that $r_c = r_a$ to reduce the number of parameters).

be supported by the fact that the bottom layers show a lower R_{sheet} and a stronger dependency on the applied P doses than the top layers.

Our results indicate that the SMM technique is capable of detecting a region of patterned phosphorus (P) with as few as 1900 or 4200 densely packed atoms, buried 4 or 15 nm below the silicon surface, respectively. Because we are sensing the capacitance formed between the tip and the P layer, we expect the sensitivity to scale inversely with the depth of the structures, implying that of order 10^3 P atoms, corresponding to an area of 25×25 nm^2, can be detected at a 1-nm depth, and 10^6 atoms at 100-nm depth (see fig. S6). These are remarkably small numbers, given that the sample does not have to be destroyed to achieve the measurement, as is the case for TEM or atom probe tomography. Other techniques, such as SIMS, which is generally regarded as a highly sensitive element-specific technique, cannot be used at all to measure the properties of these buried nanostructures. As mentioned earlier, the scanning dc or low-frequency capacitance microscopy technique can potentially image the same number of dopants; however, it cannot provide the depth and electrical information of SMM. The current interest in noninvasive imaging is highlighted by a very recent paper, which describes the use of

a near-field terahertz imaging technique to image a printed circuit board on the underside of a 115-μm-thick silicon wafer (46). However, the technique only has a lateral resolution of ~100 μm, over three orders of magnitude coarser than the SMM.

The results presented here open up exciting opportunities for dopant nanostructure fabrication by providing a measurement capability not possible with any other technique. Besides localizing dopants in three dimensions, SMM accesses the intrinsic electrical properties of the δ layers. In addition, being nondestructive, it can be implemented within the same scanning probe instrument used to pattern the devices, which allows in situ and iterative control during the entire lithography/molecular beam epitaxy (MBE) process for atomic-scale deterministic doping. This ability will be especially useful to speed up the current development of 3D patterned device structures (47) and significantly aid in the interpretation of their electrical transport behavior. One of the several exciting applications that could emerge from our research is the use of SMM as a diagnostic for the development of a surface code quantum computer (SCQC) (2, 3). In the SCQC proposed by Hill et al. (2), the single dopant qubits are manipulated and read out using single-electron transistors (SETs) and a crossbar array of electrodes. Both the SETs and the arrays are fabricated from precisely placed arrays of dopants, below the silicon surface, on three separate layers. With further expected improvements in the SMM technique, direct imaging SETs and electrodes would be possible.

MATERIALS AND METHODS
Sample preparation
The P δ-layer nanostructures were fabricated using an Omicron VT-STM system with a base pressure of less than 2×10^{-10} mbar. Samples with a size of 9×2 mm^2 were diced from an n-type arsenic-doped Si(100) wafer (15 ohm·cm and 500 μm in thickness). The Si surface was cleaned and passivated with hydrogen in ultrahigh vacuum using a standard process (41). Briefly, patterns of clean Si were written by depassivating the Si(100)-2 × 1:H surface (48) using the electron beam from an STM tip. Exposing the patterned surface to a background PH$_3$ pressure of ~1×10^{-9} mbar for 2 min [0.09 Langmuir (L)] resulted in adsorption of the PH$_3$ molecules exclusively within the depassivated regions (49). The phosphorus atoms were incorporated into the surface via a 2-min anneal at 350°C (40), and subsequently the donor nanostructure was encapsulated with 15 nm of silicon, grown by MBE from a Si sublimation source. A low sample temperature of ≈250°C during the Si sublimation provided both a low donor surface segregation and relatively smooth Si crystal growth (35).

The 3D P δ-layer structure had been fabricated using a similar method to that used for the first sample. After depassivating an area of 3.5×0.5 μm for the first bar, the surface was exposed to a PH$_3$ saturation dosage of 0.09 L. This procedure was subsequently repeated for the second (0.003 L) and third (0.002 L) bars. After an incorporation anneal for 2 min at 350°C, the sample had been encapsulated with 5 nm of silicon. For the first 10 monolayers the sample temperature was kept at low temperatures (around 60°C) to suppress P segregation [the use of a so-called "locking layer," as described by Keizer et al. (44)], followed by a rapid thermal anneal of 15 s at 500°C and a lower silicon encapsulation temperature of 250°C with a rate of 1 monolayers per minute. After reaching the estimated final encapsulation thickness of 5 nm, a 2-min anneal to 450°C led to a low surface roughness, ensuring a high-quality H passivation for the second δ-layer patterning. The bars in the top layer had been written and dosed with

the same parameters as those in the bottom layer but were rotated by 90°.

Growth calibration by δ-layer samples

To establish appropriate growth parameters, we performed a separate series of sample preparation and characterization steps on phosphorus δ-layer samples: These were the samples where an entire substrate was exposed to phosphine without any H passivation or lithographic patterning steps. The samples were overgrown with 15 nm of epitaxial silicon in the same way as for the nanostructured samples.

SIMS measurements on these δ-layer samples determined the thickness of the Si capping layer to be 14.45 ± 0.01 nm. Hall bar measurements of buried active P δ layers grown using the same PH_3 background pressure and exposure time determined a sheet dopant density of $(2.87 \pm 0.03) \times 10^{14}$ cm^{-2} for a PH_3 saturation dosage of 0.09 L, $(6.23 \pm 0.03) \times 10^{13}$ cm^{-2} for a dose of 0.003 L, and $(1.86 \pm 0.03) \times 10^{13}$ for a dose of 0.002 L, respectively, which is consistent with previous reports (40). These values corresponded to donor densities of $(4.7 \pm 0.05) \times 10^{21}$ cm^{-3}, $(1.0 \pm 0.05) \times 10^{21}$ cm^{-3}, and $(0.3 \pm 0.05) \times 10^{21}$ cm^{-3}, respectively.

SMM setup and calibration

A commercial transmission line SMM consisting of a standard 5600 AFM interfaced with a 20-GHz VNA was used (both from Keysight Technologies). Soft ($k = 0.3$ N/m) solid platinum AFM tips (Rocky Mountain Nanotechnology) were chosen to reduce the contact force and maintain a sharp tip. The AFM tip was used as a nanoscale imaging and microwave probe, enabling simultaneous topographic and electromagnetic characterization of the sample. We used contact mode for the xy scans reported in this paper. The VNA measured the ratio of the incident and the reflected signal at the tip, the so-called scattering S_{11} parameter. To transform the high impedance of the tip-sample contact to the sensitive 50 ohms of the VNA, a half-wavelength coaxial resonator in conjunction with a 50-ohm shunt resistor was used (50). Measurements were performed at frequencies between 18 and 20 GHz.

To convert measured reflection S_{11} values into capacitance values, we applied the calibration procedure recently proposed by Gramse et al. (13). The measured reflection coefficient S_{11} was converted into the complex impedance Z using the one-port black-box calibration. The defined calibration standards to calculate three complex error parameters e_{00}, e_{01}, and e_{11} were provided by simultaneously acquiring EFM and S_{11} approach curves. For this, the tip approached the surface until it made contact, and both the EFM-dC/dz and the S_{11} signals were recorded. No external capacitance calibration sample was required. The main advantages of this approach are that it works in situ on the sample under test, making a specific calibration sample redundant.

SUPPLEMENTARY MATERIALS

Supplementary material for this article is available at http://advances.sciencemag.org/cgi/content/full/3/6/e1602586/DC1

section S1. Selection of measurement frequency
section S2. FEM for the extraction of conductivity and depth of dopant layer
section S3. Dopant distribution
section S4. Lateral/vertical resolution and sensitivity
fig. S1. Frequency sensitivity analysis.
fig. S2. SMM approach curve for electrical tip calibration.
fig. S3. Finite width of P-layer distribution.
fig. S4. SIMS measurement of phosphorus and oxygen on a 3D sample for verification of dopant depth.
fig. S5. Topography and SMM capacitance image of 3D sample.

fig. S6. Lateral resolution from STM and SMM capacitance.
fig. S7. Lateral SMM capacitance resolution for increasing tip radii.

REFERENCES AND NOTES

1. International Technology Roadmap for Semiconductors-ITRS 2.0 (2015); www.itrs2.net.
2. C. D. Hill, E. Peretz, S. J. Hile, M. G. House, M. Fuechsle, S. Rogge, M. Y. Simmons, L. C. L. Hollenberg, A surface code quantum computer in silicon. Sci. Adv. 1, e1500707 (2015).
3. G. Pica, B. W. Lovett, R. N. Bhatt, T. Schenkel, S. A. Lyon, Surface code architecture for donors and dots in silicon with imprecise and nonuniform qubit couplings. Phys. Rev. B 93, 035306 (2016).
4. K. E. J. Goh, L. Oberbeck, M. Y. Simmons, A. R. Hamilton, M. J. Butcher, Influence of doping density on electronic transport in degenerate Si:P δ-doped layers. Phys. Rev. B 73, 035401 (2006).
5. F. J. Ruess, L. Oberbeck, M. Y. Simmons, K. E. J. Goh, A. R. Hamilton, T. Hallam, S. R. Schofield, N. J. Curson, R. G. Clark, Toward atomic-scale device fabrication in silicon using scanning probe microscopy. Nano Lett. 4, 1969–1973 (2004).
6. H. Büch, M. Fuechsle, W. Baker, M. G. House, M. Y. Simmons, Quantum dot spectroscopy using a single phosphorus donor. Phys. Rev. B 92, 235309 (2015).
7. L. Oberbeck, T. C. G. Reusch, T. Hallam, S. R. Schofield, N. J. Curson, M. Y. Simmons, Imaging of buried phosphorus nanostructures in silicon using scanning tunneling microscopy. Appl. Phys. Lett. 104, 253102 (2014).
8. M. J. Cadena, R. Misiego, K. C. Smith, A. Avila, B. Pipes, R. Reifenberger, A. Raman, Sub-surface imaging of carbon nanotube-polymer composites using dynamic AFM methods. Nanotechnology 24, 135706 (2013).
9. O. A. Castañeda-Uribe, R. Reifenberger, A. Raman, A. Avila, Depth-sensitive subsurface imaging of polymer nanocomposites using second harmonic Kelvin probe force microscopy. ACS Nano 9, 2938–2947 (2015).
10. E. Bussmann, M. Rudolph, G. S. Subramania, S. Misra, S. M. Carr, E. Langlois, J. Dominguez, T. Pluym, M. P. Lilly, M. S. Carroll, Scanning capacitance microscopy registration of buried atomic-precision donor devices. Nanotechnology 26, 085701 (2015).
11. J. Hoffmann, G. Gramse, J. Niegemann, M. Zeier, F. Kienberger, Measuring low loss dielectric substrates with scanning probe microscopes. Appl. Phys. Lett. 105, 013102 (2014).
12. K. Lai, W. Kundhikanjana, M. A. Kelly, Z. X. Shen, Calibration of shielded microwave probes using bulk dielectrics. Appl. Phys. Lett. 93, 123105 (2008).
13. G. Gramse, M. Kasper, L. Fumagalli, G. Gomila, P. Hinterdorfer, F. Kienberger, Calibrated complex impedance and permittivity measurements with scanning microwave microscopy. Nanotechnology 25, 145703 (2014).
14. C. Gao, X.-D. Xiang, Quantitative microwave near-field microscopy of dielectric properties. Rev. Sci. Instrum. 69, 3846 (1998).
15. S. Berweger, J. C. Weber, J. John, J. M. Velazquez, A. Pieterick, N. A. Sanford, A. V. Davydov, B. Brunschwig, N. S. Lewis, T. M. Wallis, P. Kabos, Microwave near-field imaging of two-dimensional semiconductors. Nano Lett. 15, 1122–1127 (2015).
16. A. Imtiaz, T. M. Wallis, P. Kabos, Near-field scanning microwave microscopy: An emerging research tool for nanoscale metrology. IEEE Microwave Mag. 15, 52–64 (2014).
17. W. Kundhikanjana, K. Lai, H. Wang, H. Dai, M. A. Kelly, Z.-x. Shen, Hierarchy of electronic properties of chemically derived and pristine graphene probed by microwave imaging. Nano Lett. 9, 3762–3765 (2009).
18. E. Brinciotti, G. Gramse, S. Hommel, T. Schweinboeck, A. Altes, M. A. Fenner, J. Smoliner, M. Kasper, G. Badino, S.-S. Tuca, F. Kienberger, Probing resistivity and doping concentration of semiconductors at the nanoscale using scanning microwave microscopy. Nanoscale 7, 14715–14722 (2015).
19. A. Imtiaz, T. M. Wallis, S.-H. Lim, H. Tanbakuchi, H.-P. Huber, A. Hornung, P. Hinterdorfer, J. Smoliner, F. Kienberger, P. Kabos, Frequency-selective contrast on variably doped p-type silicon with a scanning microwave microscope. J. Appl. Phys. 111, 093727 (2012).
20. K. Lai, W. Kundhikanjana, M. Kelly, Z. X. Shen, Modeling and characterization of a cantilever-based near-field scanning microwave impedance microscope. Rev. Sci. Instrum. 79, 063703 (2008).
21. D. Wu, X. Li, L. Luan, X. Wu, W. Li, M. N. Yogeesh, R. Ghosh, Z. Chu, D. Akinwande, Q. Niu, K. Lai, Uncovering edge states and electrical inhomogeneity in MoS₂ field-effect transistors. Proc. Natl. Acad. Sci. U.S.A. 113, 8583–8588 (2016).
22. A. Lenk, H. Lichte, U. Muehle, 2D-mapping of dopant distribution in deep sub micron CMOS devices by electron holography using adapted FIB-preparation. J. Electron Microsc. 54, 351–359 (2005).
23. V. C. Holmberg, J. R. Helps, K. A. Mkhoyan, D. J. Norris, Imaging impurities in semiconductor nanostructures. Chem. Mater. 25, 1332–1350 (2013).
24. P. C. Zalm, Ultra-shallow doping profiling with SIMS. Rep. Prog. Phys. 58, 1321–1374 (1995).

25. D. W. van der Weide, P. Neuzil, The nanoscilloscope: Combined topography and AC field probing with a micromachined tip. *J. Vac. Sci. Technol. B* **14**, 4144–4147 (1996).

26. C. Gao, T. Wei, F. Duewer, Y. Lu, X.-D. Xiang, High spatial resolution quantitative microwave impedance microscopy by a scanning tip microwave near-field microscope. *Appl. Phys. Lett.* **71**, 1872 (1997).

27. H. P. Huber, M. Moertelmaier, T. M. Wallis, C. J. Chiang, M. Hochleitner, A. Imtiaz, Y. J. Oh, K. Schilcher, M. Dieudonne, J. Smoliner, P. Hinterdorfer, S. J. Rosner, H. Tanbakuchi, P. Kabos, F. Kienberger, Calibrated nanoscale capacitance measurements using a scanning microwave microscope. *Rev. Sci. Instrum.* **81**, 113701 (2010).

28. K. Lai, M. B. Ji, N. Leindecker, M. A. Kelly, Z. X. Shen, Atomic-force-microscope-compatible near-field scanning microwave microscope with separated excitation and sensing probes. *Rev. Sci. Instrum.* **78**, 063702 (2007).

29. C. P. Vlahacos, R. C. Black, S. M. Anlage, A. Amar, F. C. Wellstood, Near-field scanning microwave microscope with 100 μm resolution. *Appl. Phys. Lett.* **69**, 3272–3274 (1996).

30. A. Tselev, S. M. Anlage, Z. Ma, J. Melngailis, Broadband dielectric microwave microscopy on micron length scales. *Rev. Sci. Instrum.* **78**, 044701 (2007).

31. M. Farina, A. Lucesoli, T. Pietrangelo, A. di Donato, S. Fabiani, G. Venanzoni, D. Mencarelli, T. Rozzi, A. Morini, Disentangling time in a near-field approach to scanning probe microscopy. *Nanoscale* **3**, 3589–3593 (2011).

32. Y. Ren, H. Yuan, X. Wu, Z. Chen, Y. Iwasa, Y. Cui, H. Y. Hwang, K. Lai, Direct imaging of nanoscale conductance evolution in ion-gel-gated oxide transistors. *Nano Lett.* **15**, 4730–4736 (2015).

33. G. Gramse, E. Brinciotti, A. Lucibello, S. B. Patil, M. Kasper, C. Rankl, R. Giridharagopal, P. Hinterdorfer, R. Marcelli, F. Kienberger, Quantitative sub-surface and non-contact imaging using scanning microwave microscopy. *Nanotechnology* **26**, 135701 (2015).

34. S. R. McKibbin, W. R. Clarke, M. Y. Simmons, Investigating the surface quality and confinement of Si:P δ-layers at different growth temperatures. *Physica E* **42**, 1180–1183 (2010).

35. S. R. McKibbin, W. R. Clarke, A. Fuhrer, T. C. G. Reusch, M. Y. Simmons, Investigating the regrowth surface of Si:P δ-layers toward vertically stacked three dimensional devices. *Appl. Phys. Lett.* **95**, 233111 (2009).

36. S. M. Sze, K. K. Ng, *Physics of Semiconductor Devices* (John Wiley and Sons, ed. 3, 2006).

37. L. Fumagalli, G. Gramse, D. Esteban-Ferrer, M. A. Edwards, G. Gomila, Quantifying the dielectric constant of thick insulators using electrostatic force microscopy. *Appl. Phys. Lett.* **96**, 183107 (2010).

38. G. Gramse, G. Gomila, L. Fumagalli, Quantifying the dielectric constant of thick insulators by electrostatic force microscopy: Effects of the microscopic parts of the probe. *Nanotechnology* **23**, 205703 (2012).

39. Rocky Mountain Nanotechnology, Technical Data Sheet (2016); http://rmnano.com/tech.html.

40. L. Oberbeck, N. J. Curson, M. Y. Simmons, R. Brenner, A. R. Hamilton, S. R. Schofield, R. G. Clark, Encapsulation of phosphorus dopants in silicon for the fabrication of a quantum computer. *Appl. Phys. Lett.* **81**, 3197–3199 (2002).

41. J. L. O'Brien, S. R. Schofield, M. Y. Simmons, R. G. Clark, A. S. Dzurak, N. J. Curson, B. E. Kane, N. S. McAlpine, M. E. Hawley, G. W. Brown, Towards the fabrication of phosphorus qubits for a silicon quantum computer. *Phys. Rev. B* **64**, 161401(R) (2001).

42. D. F. Sullivan, B. E. Kane, P. E. Thompson, Weak localization thickness measurements of Si:P delta-layers. *Appl. Phys. Lett.* **85**, 6362–6364 (2004).

43. B. Weber, S. Mahapatra, H. Ryu, S. Lee, A. Fuhrer, T. C. G. Reusch, D. L. Thompson, W. C. T. Lee, G. Klimeck, L. C. L. Hollenberg, M. Y. Simmons, Ohm's law survives to the atomic scale. *Science* **335**, 64–67 (2012).

44. J. G. Keizer, S. Koelling, P. M. Koenraad, M. Y. Simmons, Suppressing segregation in highly phosphorus doped silicon monolayers. *ACS Nano* **9**, 12537–12541 (2015).

45. W. R. Clarke, X. J. Zhou, A. Fuhrer, T. C. G. Reusch, M. Y. Simmons, The effect of surface proximity on electron transport through ultra-shallow δ-doped layers in silicon. *Physica E* **40**, 1566–1568 (2008).

46. R. I. Stantchev, B. Sun, S. M. Hornett, P. A. Hobson, G. M. Gibson, M. J. Padgett, E. Hendry, Noninvasive, near-field terahertz imaging of hidden objects using a single-pixel detector. *Sci. Adv.* **2**, e1600190 (2016).

47. J. G. Keizer, S. R. McKibbin, M. Y. Simmons, The impact of dopant segregation on the maximum carrier density in Si:P multilayers. *ACS Nano* **9**, 7080–7084 (2015).

48. D. P. Adams, T. M. Mayer, B. S. Swartzentruber, Nanometer-scale lithography on Si(001) using adsorbed H as an atomic layer resist. *J. Vac. Sci. Technol. B* **14**, 1642–1649 (1996).

49. T.-C. Shen, J.-Y. Ji, M. A. Zudov, R.-R. Du, J. S. Kline, J. R. Tucker, Ultradense phosphorous delta layers grown into silicon from PH₃ molecular precursors. *Appl. Phys. Lett.* **80**, 1580–1582 (2002).

50. H. Tanbakuchi, M. Richter, F. Kienberger, H. P. Huber, Nanoscale materials and device characterization via a scanning microwave microscope, in *2009 IEEE International Conference on Microwaves, Communications, Antennas and Electronics Systems (COMCAS'09)*, (IEEE, 2009), pp. 1–4.

Science Advances

Nondestructive imaging of atomically thin nanostructures buried in silicon

Georg Gramse, Alexander Kölker, Tingbin Lim, Taylor J. Z. Stock, Hari Solanki, Steven R. Schofield, Enrico Brinciotti, Gabriel Aeppli, Ferry Kienberger and Neil J. Curson

ARTICLE TOOLS	http://advances.sciencemag.org/content/3/6/e1602586
SUPPLEMENTARY MATERIALS	http://advances.sciencemag.org/content/suppl/2017/06/26/3.6.e1602586.DC1
REFERENCES	This article cites 46 articles, 5 of which you can access for free http://advances.sciencemag.org/content/3/6/e1602586#BIBL
PERMISSIONS	http://www.sciencemag.org/help/reprints-and-permissions

Use of this article is subject to the Terms of Service